# Comparing non-tidal ocean loading around the southern North Sea with subdaily GPS/GLONASS data

**Jianghui Geng**[1], **Shaoming Xin**[1], **Simon D P Williams**[2], **Weiping Jiang**[1]

[1]GNSS Research Center, Wuhan University, China

[2]National Oceanography Centre, UK

**Key Points:**

- GNSS displacements were compared with non-tidal ocean loading predictions at 18 coastal stations
- The loading displacements due to peak storm surges are identified using subdaily GNSS
- The principal component analysis improves subdaily GNSS in resolving the loading signatures

Corresponding author: Jianghui Geng, jgeng@whu.edu.cn

**Abstract**

Observing subdaily surface deformations is important to the interpretation of rapidly developing transient events. However, it is not known whether GNSS (Global Navigation Satellite System) is able to identify millimeter-level transient displacements over various subdaily timescales. We studied non-tidal ocean loading (NTOL) using 18 GNSS stations along the southern North Sea for November–December 2013, and compared 3-hourly GPS/GLONASS displacements with NTOL predictions. It was found that they overall agreed well with a mean correlation coefficient of 0.6 and their vertical differences had an RMS of 5.7 mm, but a 10-mm subsidence prediction for December 5th could only be marginally detected. Hence the spatial coherence among the loading signatures at the 18 stations was harnessed to improve subdaily GNSS, and then the predicted displacements of 5–10-mm over the subdaily timescales could be discriminated successfully. We envision that adding Galileo/BeiDou signals to GPS/GLONASS can further improve the resolution of subdaily GNSS, which can also enhance the spatial coherence of transient signals captured by regional GNSS stations.

## 1 Introduction

The GPS (Global Positioning System) has been used comprehensively to unravel the characteristics of Earth crustal motions. A norm of GPS processing for geophysics is that 24 hours of raw carrier-phase and pseudorange data are reduced to daily positions aligned with a temporally stable reference frame (Herring et al., 2016). It has been recognized that daily GPS can achieve the positioning precision of a few millimeters (*e.g.*, Bos et al., 2013; Rebischung et al., 2016). Such positions can ultimately play an indispensable role in exploring the subtle surface deformations continuing over months, years and decades, such as inter-seismic displacements across active faults, tectonic movements along plate boundaries as well as environmental loading caused by mass redistributions (*e.g.*, Hammond et al., 2016; Shen et al., 2011; van Dam et al., 2017). However, there are varieties of crustal motion events which are characterized predominantly by subdaily transient displacements spanning typically tens of minutes to a few hours, *e.g.*, pre-eruption volcanic unrest, early post-seismic relaxation, etc. (*e.g.*, Malservisi et al., 2015; Prates et al., 2013; Twardzik et al., 2019). These events cannot be measured using daily GPS due to its insufficient temporal resolution.

High-rate GPS, sampling data at more than once per second, can be a viable solution to the deficient temporal resolution of daily GPS. High-rate GPS was originally used to capture seismic waveforms which usually span seconds to minutes (*e.g.*, Larson et al., 2003). Though high-rate GPS complements inertial sensors by measuring displacements directly over a broad frequency band, it suffers from a few orders of magnitude higher noise than conventional seismograph (*e.g.*, Bock et al., 2011). In particular, epoch-wise GPS displacements normally reach centimeter-level precisions for the horizontal components and 5–10 cm for the vertical, where the major error sources are multipath effects and atmospheric refractions (Geng et al., 2017). To improve the resolution capability of epoch-wise GPS in discerning volcanic motions, Larson et al. (2010) fine tuned the random-walk process noise of position parameters, or in other words the constraints imposed upon neighboring epochs, in a Kalman filter to suppress multipath and atmosphere contaminations. However, we should be cautious of changing such process noise arbitrarily, since the signal of interest tends to be dampened in case of super tight constraints between epochs. To address this potential risk, Penna et al. (2015) and Martens et al. (2016a) carried out synthetic tests to investigate the resolution of epoch-wise GPS in identifying ocean tidal loading (OTL) signals, before finalizing the choice for appropriate process noise. Reuveni et al. (2012) further corrected epoch-wise GPS for the predetermined tropospheric delays from daily GPS (*e.g.*, Bilich et al., 2008; Choi et al., 2004). The resolution of subdaily displacements was then improved by a factor of around 2–5, but with a risk that the vertical motion signals can leak into the tropospheric estimates (Penna et al., 2015).

Most research to date on subdaily signals has focused exclusively on only GPS; the advent of multi-GNSS (Global Navigation Satellite System) data provides an appealing opportunity to improve the resolution of epoch-wise displacements. As an initial trial, Geng et al. (2017) integrated 1-Hz GLONASS (GLObalnaya NAvigatsionnaya Sputnikovaya Sistema) with GPS data in point solutions to measure seismic signals, and found that the precision of the north component was improved markedly by up to 40% thanks to the higher inclination of GLONASS orbital planes. Abbaszadeh et al. (2020) found that GLONASS data were able to measure the OTL heights at the luni-solar semi-diurnal and diurnal periods at a resolution of 2.0 mm compared to 4.4 mm ($2\sigma$) in the case of GPS data (see also Matviichuk et al., 2020). Geng et al. (2018) further applied orbital repeat time (ORT) filtering, an upgraded version of GPS sidereal filtering, on an inte-

grated high-rate GPS/GLONASS/BeiDou-2 solution to alleviate multipath effects. It was reported that the precision of all three components could be improved by 30-60% compared to GPS-only solutions over the periods of a few seconds to half a day. Overall, high-rate multi-GNSS was able to measure displacements with repeatability of 0.4, 0.4 and 1.3 cm for the east, north and up components, respectively, in terms of RMS error ($1\sigma$) over a 24-hour span.

However, few studies have demonstrated over what subdaily timescales the GNSS displacements suffice to discriminate a transient geophysical signal of diverse and rich frequency content against a colored noise background (*e.g.*, King et al., 2008). In this study, we investigate the resolution of subdaily GNSS by identifying the non-tidal ocean loading (NTOL) displacements taking place throughout November–December 2013 around the southern North Sea of Europe. An NTOL model based on meteorological input is compared with the subdaily GNSS solutions. We will study how the GPS/GLONASS integration can improve subdaily GNSS positioning precision in the framework of a time-frequency domain (Torrence & Compo, 1998). Next, we inspect how the spatial coherence of displacements across a regional GNSS network can be exploited to improve subdaily GNSS, as well as the potential risk of presuming such spatial coherence to geophysical processes (Dong et al., 2006).

## 2 Non-tidal ocean loading

Often predominantly during the winter, strong winds originating from low pressure systems over the northern Atlantic repeatedly drive the North Sea water towards the narrow English Channel and German bight, leading to a storm surge event (Spencer et al., 2015). While preceded and followed by a number of minor storm surges through November–December 2013, one extreme event occurring on December 5–6 was the largest recorded since 1953. The wind speed was over 100 km/h across Scotland, pushing the sea level to rise by 2 m at Lowestoft tide gauge (Spencer et al., 2015). The surge water propagated southwards along the eastern coast of Britain, then continued striking the northern coasts of Belgium and Netherlands and finally receded close to North Germany and Denmark. As a result, the excess water trapped in the southern North Sea caused the seafloor to subside and the land around to tilt towards the sea in accordance with the elastic Earth response to mass redistributions (*e.g.*, van Dam et al., 2012). This phe-

nomenon, caused by storm surges, is categorized as NTOL. It repeatedly affects eastern England, northern Belgium and Netherlands in winter seasons (Geng et al., 2012).

For a better preparedness against the flooding caused by storm surges, the Proudman Oceanographic Laboratory (now part of the National Oceanography Centre) in the UK developed a barotropic storm surge model (POLSSM) to forecast the sea level elevations every hour across the North Sea by ingesting the surface wind stress and atmospheric pressure from a weather forecast model provided by UK Meteorological Office (www.ntslf.org) (Flather, 2000). The model covers the oceanic water from 48°N to 63°N and from 12°W to 13°E, divided into regular grids every 0.11° in latitude and 0.16° in longitude (Fig. 1) (Fratepietro et al., 2006). We convolved the hourly sea level distribution with the Green's functions (GFs) derived from the PREM (Preliminary Reference Earth Model) using the SPOTL software to obtain the 3-dimensional (3D) displacements of coastal stations in the center of mass of the solid Earth (CE) frame, which are here termed as NTOL predictions throughout (Agnew, 1997; Dziewonski & Anderson, 1981; Farrell, 1972; Williams & Penna, 2011). Note that GNSS displacements over non-secular timescales are in the center of figure of the outer surface of the solid Earth (CF) frame, which is close to CE since their difference is as minimal as 2% of the geocenter motion (Blewitt, 2003; Dong et al., 2003).

Fig. 1 displays two snapshot displacement fields during 21:00–22:00 UT on December 5 and 0:00–01:00 UT on December 6, 2013. The sea level distribution was more spatially variable over 21:00–22:00 in contrast to that over 0.00–01:00 despite their temporal separation of only 2 hours. Specifically, during 0:00–01:00 the sea level anomaly peaked to over 2 m near the shores of Netherlands and the coast was predicted to have subsided by about 30 mm. In Fig. 2, we show the NTOL predictions for November–December 2013 at 18 coastal stations shown in Fig. 3. Around day 340 (*i.e.*, December 6), the largest subsidence is 40 mm while the horizontal movements reach 5 mm at a number of stations. One conspicuous phenomenon is that the vertical displacements are near uniform across all 18 stations over the two months, despite their slightly differing magnitudes. Similar characteristics of approximate uniformity are also observed for the north component, while the east component from the stations located along the western North Sea presents a generally opposite displacement pattern to that of the stations along the eastern North Sea. It is worth noting that the North Sea is quite exceptional in producing dramatic NTOL signals due to its special geographic characteristic (*e.g.*, shallow waters,

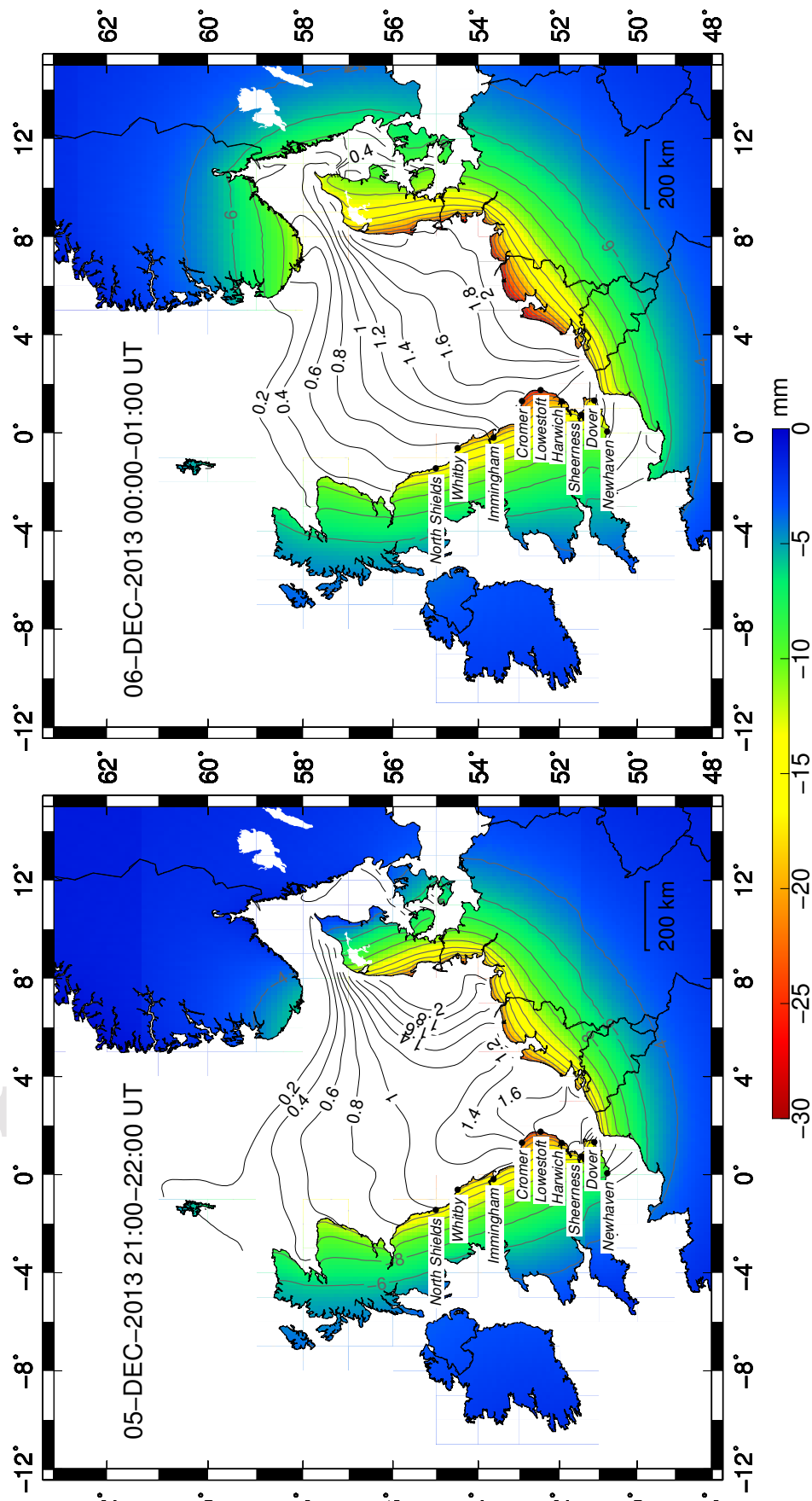


**Figure 1.** Sea level rise and ground subsidence caused by an extreme storm surge event during 21:00-22:00 on December 5 and 0:00–1:00 on December 6, 2013 in the North Sea. The water area is contoured every 0.2 m according to the sea levels while the land subsidence is color-contoured every 2 mm. The nine black solid circles denote the tide gauge stations along the eastern coast of England.

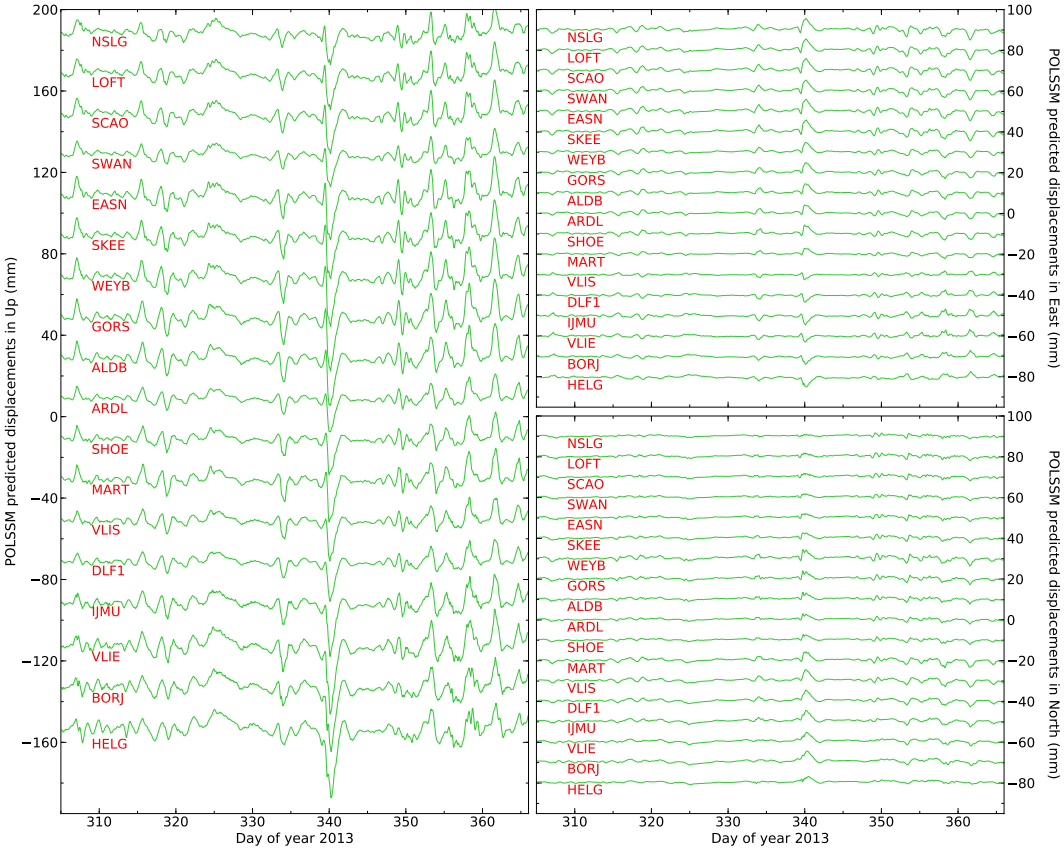


**Figure 2.** NTOL predictions (mm) in the up, east and north directions at the 18 coastal stations from November to December 2013. Each time series is offset by multiples of 10 mm to avoid overlap of symbols. All panels have the same vertical scale.

coastal morphology) that concentrates storm surges. The close proximity of the 18 stations to the southern coast also increases the probability of capturing NTOL signatures.

In theory, the errors of the NTOL predictions are primarily governed by the underlying Earth model and the forecasted sea level distribution across the North Sea. The GFs are computed based on predefined Earth models. The GF precision is thus subject to how precise the geological models can delineate the Earth's structural details (Martens et al., 2016b). Wang et al. (2012) reported that the GFs derived from various Earth models could differ by up to 10–15% for the horizontal components. Dill et al. (2015) indicated that the GFs could have an uncertainty of ±12% in the vertical and ±21% in the horizontal directions, which was attributed to the inhomogeneities of local Earth crustal structure.

**Table 1.** RMS (m) of the differences between the de-tided tide gauge data and the POLSSM predicted sea levels in November ($RMS_{Nov.}$) and December ($RMS_{Dec.}$) 2013 (reported at www.ntslf.org). The tide gauge locations refer to Fig. 1.

| **Tide gauge sites** | $\mathbf{RMS}_{\mathrm{Nov.}}$ | $\mathbf{RMS}_{\mathrm{Dec.}}$ |
|---|---|---|
| North Shields | 0.069 | 0.091 |
| Whitby | 0.114 | 0.119 |
| Immingham | 0.143 | 0.168 |
| Cromer | 0.122 | 0.163 |
| Lowestoft | 0.080 | 0.124 |
| Harwich | 0.110 | 0.165 |
| Sheerness | 0.106 | 0.176 |
| Dover | 0.092 | 0.119 |
| Newhaven | 0.079 | 0.081 |
| Mean | 0.102 | 0.134 |

On the other hand, imprecise modeling of the loading mass distribution (or sea levels across North Sea) can contribute more to the errors in ocean-loading predictions (Yuan et al., 2013). Although Fratepietro et al. (2006) showed that the formal errors of POLSSM predicted sea levels at coastal tide gauges were around 10 cm ($1\sigma$, Table 1), the error distribution across the entire North Sea is hardly known. In this study, we simply presume that the average error in POLSSM predicted sea levels across the North Sea is 10 cm, and that 30 cm bounds 99.7% ($3\sigma$) of sea level errors across all POLSSM grid points. To comprehend the impact of this error assumption on NTOL predictions, we picked all hourly sea level predictions from 2012 to 2016 whose peak-to-peak variations over all grids were less than 30 cm to mimic the error distribution of the POLSSM predictions across the North Sea. We found 2544 eligible hours in total. Next, we used the sea level predictions from these periods to approximate the errors in the NTOL predictions. Table 2 shows the NTOL prediction errors for the up, east and north components at all 18 coastal stations. Nominally, the vertical prediction errors are all within 0.5–1.0 mm (less than 5% of the predicted peak subsidence), and the horizontal errors do not exceed 0.2 mm (less than 10% of the predicted peak horizontal motions). Note that the error quantities in Table 2 are estimated with the assumption of no Earth model errors and simulated sea level errors.

**Table 2.** Nominal NTOL prediction errors (mm) in the up, east and north components at 18 coastal stations (*cf.*, Fig. 3 for the station locations). The percentages in the parentheses show the ratio between the nominal NTOL prediction errors and the predicted peak displacements at that station on December 5–6, 2013.

| **Station** | **Up** | **East** | **North** |
|---|---|---|---|
| NSLG | 0.77 (4.5%) | 0.19 (3.3%) | 0.16 (9.5%) |
| LOFT | 0.79 (4.1%) | 0.17 (3.0%) | 0.17 (8.4%) |
| SCAO | 0.81 (3.9%) | 0.18 (3.0%) | 0.17 (9.1%) |
| SWAN | 0.65 (3.8%) | 0.16 (3.0%) | 0.15 (8.3%) |
| EASN | 0.85 (3.7%) | 0.17 (2.8%) | 0.16 (7.7%) |
| SKEE | 0.78 (3.5%) | 0.16 (2.8%) | 0.16 (5.9%) |
| WEYB | 0.84 (3.3%) | 0.12 (2.4%) | 0.19 (4.3%) |
| GORS | 0.86 (3.1%) | 0.12 (2.4%) | 0.17 (4.2%) |
| ALDB | 0.79 (3.2%) | 0.11 (2.4%) | 0.15 (4.2%) |
| ARDL | 0.61 (3.5%) | 0.10 (2.4%) | 0.14 (4.6%) |
| SHOE | 0.64 (3.5%) | 0.11 (2.5%) | 0.13 (4.6%) |
| MART | 0.74 (3.4%) | 0.08 (2.8%) | 0.16 (3.8%) |
| VLIS | 0.61 (2.9%) | 0.10 (3.9%) | 0.16 (2.9%) |
| DLF1 | 0.60 (2.9%) | 0.12 (3.4%) | 0.16 (2.9%) |
| IJMU | 0.75 (2.7%) | 0.14 (3.0%) | 0.17 (3.0%) |
| VLIE | 0.96 (2.7%) | 0.11 (3.6%) | 0.18 (3.7%) |
| BORJ | 0.89 (2.6%) | 0.13 (3.3%) | 0.18 (3.2%) |
| HELG | 0.95 (2.6%) | 0.15 (3.0%) | 0.12 (3.7%) |

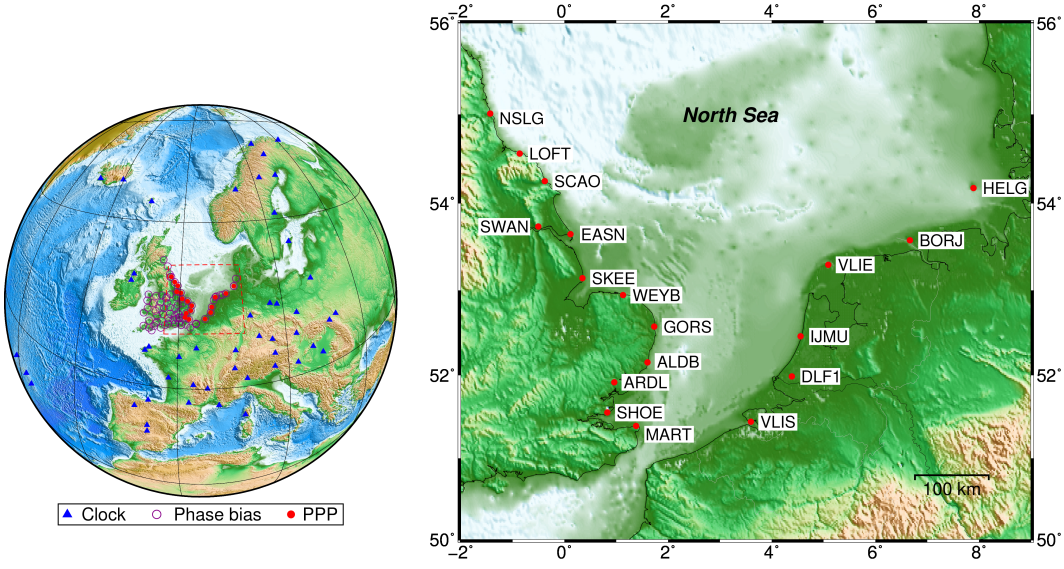


**Figure 3.** Station distribution. The left panel shows a global view of all stations where the 40 blue triangles denote those for satellite clock estimation, the 60 open purple circles denote those for GPS/GLONASS phase bias and GLONASS code-phase bias computations, and the 18 solid red circles denote those for PPP. The right panel is a close-up showing the distribution of PPP stations with site codes plotted aside.

## 3 GNSS data processing

Two months (November–December 2013) of 30-s dual-frequency GPS/GLONASS data at 18 stations across the coastal areas of eastern Britain and northern continental Europe were processed using precise point positioning (PPP) (Fig. 3) (Zumberge et al., 1997). The PRIDE PPP-AR software was used for the entire GNSS data analysis (Geng et al., 2019b). At each epoch, we could observe on average eight GPS satellites and seven GLONASS satellites. Another 40 stations were used to calculate precise satellite clock corrections and 60 more used for phase bias and code-phase bias computations to enable PPP ambiguity resolution (PPP-AR) for both GPS and GLONASS (*cf.*, Geng et al., 2019a). A cut-off angle of 10° above the horizon was set for usable GNSS observations which were later weighted according to an elevation-dependent strategy. We assigned 0.01 cycles and 0.3 m to the *a priori* noise of raw carrier-phase and pseudorange data, respectively.

The ESA/ESOC (European Space Agency/European Space Operations Centre) final satellite orbit products and Earth rotation parameters were fixed throughout the GNSS

data processing, and thus GNSS displacements in this study refer to the CF frame. The solid-earth tides and pole tides were corrected based on the IERS conventions, and the OTL corrections were computed in the CE frame based on the FES2004 model to follow IGS conventions (Lyard et al., 2006; Petit & Luzum, 2010). Notably, we also applied the atmospheric pressure loading corrections of a 6-hour interval on a 2.5°×2.5° grid using the surface pressure fields from the NCEP/NCAR (National Centers for Environmental Prediction/National Center for Atmospheric Research) reanalysis project (Williams & Penna, 2011). In addition, zenith troposphere delays (ZTDs) were *a priori* corrected using the ECMWF (European Centre for Medium-Range Weather Forecasts) derived hydrostatic and wet components; the Vienna Mapping Function 1 (VMF1) was then used to project the zenith delays onto slant directions (Boehm et al., 2006). We estimated residual ZTDs every hour and horizontal troposphere gradients every 3 hours as random-walk parameters with process noise of 2 cm/$\sqrt{hr}$ and 2 mm/$\sqrt{3hr}$, respectively. The second-order ionospheric delays were also corrected using the global ionospheric maps by CODE (Centre for Orbit Determination in Europe) (Fritsche et al., 2005; Pireaux et al., 2010). PPP-AR was attempted for all visible GPS/GLONASS satellites above the 10° elevation (Geng et al., 2019b). The fixing rates were 98.96% for GPS and 98.99% for GLONASS. We adopted a piece-wise constant positioning technique instead of epoch-wise positioning, where PPP-AR was based on 24 hours of arcs, but the positions were computed every three hours instead of every 30 s (Melbourne et al., 2002; Geng et al., 2012). The stochastic constraint between neighboring 3-hourly positions is 2 cm/$\sqrt{hr}$.

Multipath effects were also corrected throughout. We first used the IGS (International GNSS Service) precise ephemerides for November 2013 to compute the ORTs for each GPS/GLONASS satellite (Agnew & Larson, 2007). The GPS satellite ORTs ranged from 86152 to 86164 s, and the GLONASS satellite ORTs from 84455 s to 84476 s plus 7 days. Next, we carried out ORT filtering in the observation domain. Undifferenced carrier-phase residuals were computed for all involved satellites. Then the carrier-phase residuals of $n$ times of the ORT before and after the target period to be filtered were stacked and averaged for each satellite to produce the desired multipath corrections. Particularly, $n = 1, 2, \cdots 6$ for GPS and $n = 1$ for GLONASS. We had to round the satellite specific ORTs to a multiple of 30 s. Then all GPS satellites had an ORT of 86160 s and GLONASS satellites had ORTs of 84450 s or 84480 s plus 7 days. In this study, the ORTs would have an error of up to 15 s. Geng et al. (2017) showed that an ORT error of 20 s

**Table 3.** Mean RMS (mm) for the up, east and north components over the 18 coastal stations during November–December 2013. Column $\overline{\text{RMS}}_{\text{GNSS}}$ shows the mean RMS of the four sorts of GNSS displacements (*i.e.*, "G", "G-M", "GR" and "GR-M"). Column $\overline{\text{RMS}}_{\text{GNSS-NTOL}}$ shows the mean RMS of the differences between the GNSS displacements and the NTOL predictions. Column $\overline{\text{RMS}}_{\text{PCA(GNSS)-NTOL}}$ shows the mean RMS of the differences between the PCA (principal component analysis) recovered GNSS displacements and the NTOL predictions.

| **GNSS dis-** | $\overline{\text{RMS}}_{\text{GNSS}}$ | | | $\overline{\text{RMS}}_{\text{GNSS-NTOL}}$ | | | $\overline{\text{RMS}}_{\text{PCA(GNSS)-NTOL}}$ | | |
|---|---|---|---|---|---|---|---|---|---|
| **placements** | Up | East | North | Up | East | North | Up | East | North |
| **G** | 8.7 | 2.3 | 2.7 | 7.4 | 2.2 | 2.5 | 4.3 | 1.6 | 1.6 |
| **G-M** | 8.1 | 2.1 | 2.3 | 6.5 | 2.0 | 2.1 | 3.9 | 1.5 | 1.4 |
| **GR** | 7.6 | 2.2 | 2.3 | 6.0 | 2.1 | 2.2 | 3.9 | 1.6 | 1.5 |
| **GR-M** | 7.4 | 2.0 | 2.1 | 5.7 | 1.9 | 2.0 | 3.9 | 1.5 | 1.4 |

led to an error of up to 10% over the periods of tens of seconds. We also tried an ORT of 86130 s or 86190 s for GPS-only solutions and the RMS of the 3-hourly displacements were changed negligibly by 0.2%–0.3%. Finally, the multipath corrections were low pass filtered at a cut-off period of 90 s before applied to carrier-phase data.

In addition, it may be argued that the 30-s sampling causes aliasing of higher-frequency (*i.e.*, >0.017 Hz) noise into the multipath corrections above. Geng et al. (2017) showed that multipath effects can extend to the periods of 10 s (or 0.1 Hz) and Dong et al. (2016) found that such high-frequency multipath could be very significant in the case of potent far-field reflectors. However, high-frequency noise components within high-rate GNSS displacements at fiducial stations are usually of modestly low amplitudes in contrast to those spreading over the lower-frequency bands. Typically, Geng et al. (2018) showed that the noise amplitude over the 10-s period accounted for only 30% of that over the 30-s period on average. Throughout we presume that the aliasing due to higher-frequency (*i.e.*, >0.017 Hz) multipath is negligible compared to the amplitudes of multipath residing over the longer-period bands (*e.g.*, tens of minutes to a few hours) (Smalley Jr., 2009).

# 4 Results

## 4.1 Time domain analysis

We first estimated the raw GPS displacements and then those corrected for multipath effects, which are designated as G and G-M, respectively. Correspondingly, the raw GPS/GLONASS displacements as well as those corrected for multipath effects are abbreviated as GR and GR-M, respectively. All GNSS displacements were demeaned and detrended against the NTOL predictions before computing their RMS errors (*i.e.*, $\mathrm{RMS}_{\mathrm{GNSS}}$). Hourly NTOL predictions were averaged every three hours and then deducted from the GNSS displacements to compute $\mathrm{RMS}_{\mathrm{GNSS\text{-}NTOL}}$. Table 3 shows these RMS statistics for the GPS-only and GPS/GLONASS solutions.

Column $\overline{\mathrm{RMS}}_{\mathrm{GNSS}}$ in Table 3 compares the mean RMS of the four solutions over the 18 coastal stations in November–December 2013. The G displacements have a mean RMS of 8.7, 2.3 and 2.7 mm for the up, east and north components, respectively, which reflect the contribution of varieties of signals and noise including NTOL. The ORT filtering to mitigate multipath (*i.e.*, G-M) reduces the RMS of all three components by 7–15%. In the meantime, the GPS/GLONASS integration alone (*i.e.*, GR), without multipath corrections, decreases the RMS to 7.6, 2.2 and 2.3 mm for the up, east and north components, respectively, which outperform the G-M RMS in the vertical while match them in the horizontal components. This result demonstrates the advantage of multi-GNSS over not only the GPS-only solutions, but also the cumbersome ORT filtering (Geng et al., 2017). This advantage in addressing multipath effects can also be seen in the $\overline{\mathrm{RMS}}_{\mathrm{GNSS\text{-}NTOL}}$ column. However, the ORT filtering can still benefit the GR solutions, though the RMS reductions are less than 10% as revealed by the GR-M solutions in Table 3.

The NTOL predictions and the GNSS displacements for station ALDB during December 2013 are shown in Fig. 4 (those for the remaining 17 stations refer to Figs. S1-S17). All vertical GNSS displacements (black curves) in the left panels show a large downward motion of about 25 mm around day 340. They agree generally well in both phase and amplitude with the NTOL predictions (green curves), as corroborated by their correlation coefficients (*cf.*, "CC") of 0.60–0.75 over the month. However, a visual inspection shows that the G displacements are noisier than the other three when compared to the vertical NTOL predictions. We computed the RMS of the differences between the vertical GNSS displacements and the NTOL predictions, as shown in the top-left cor-

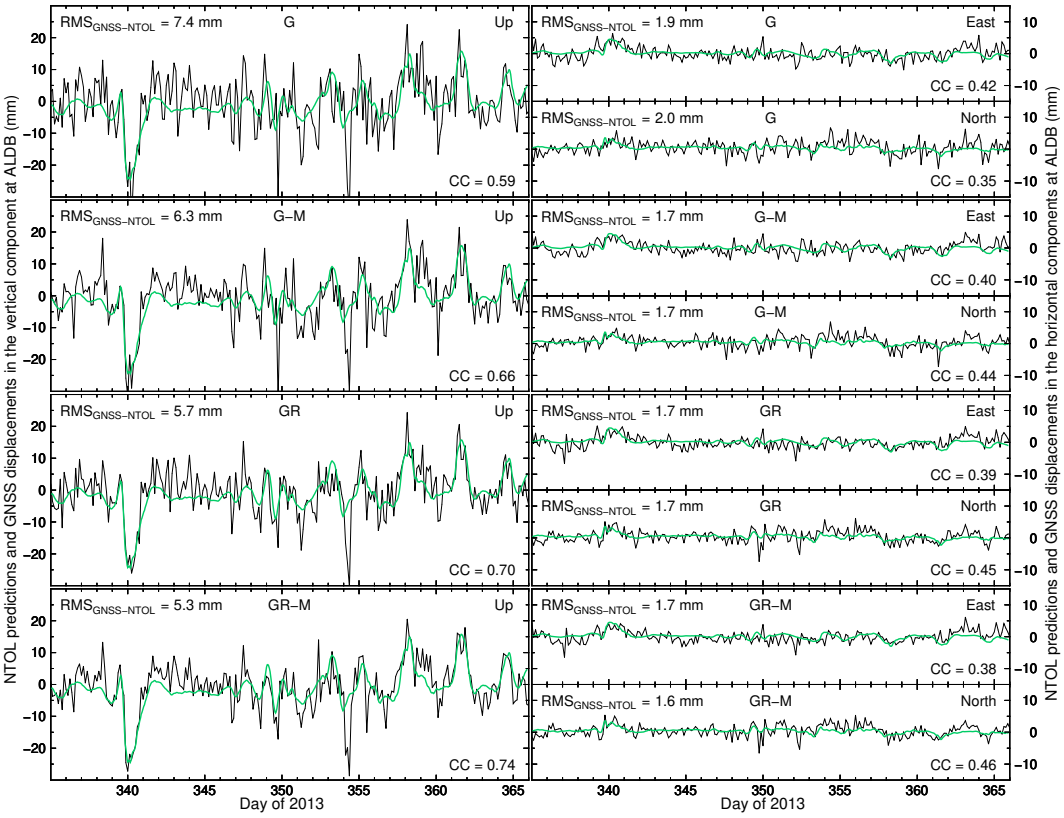


**Figure 4.** Displacements (mm) for the up, east and north components for four sorts of GNSS solutions (*i.e.*, "G", "G-M", "GR" and "GR-M") at station ALDB during December 2013. The black and green curves denote the 3-hourly GNSS displacements and the hourly NTOL predictions, respectively. "$RMS_{GNSS-NTOL}$" and "CC" denote the RMS of differences and the correlation coefficients, respectively, between the GNSS displacements and the NTOL predictions.

ner of all panels. Although the multipath corrections reduce the RMS error from 7.4 mm for the G solution to 6.3 mm for the G-M solution, the GPS/GLONASS integration (*i.e.*, GR) decreases the RMS error even further to 5.7 mm. Compared to the vertical G-M displacements, the GR displacements have smaller spikes, which is ascribed to a more robust solution where more satellites are involved (*cf.*, Geng et al., 2018). This indicates that the vertical NTOL signals appear increasingly significant when more GNSS satellites are involved.

On the contrary, though the NTOL model also predicts a displacement of up to 5 mm for the horizontal components at ALDB around day 340, this motion can only be marginally detected within the GNSS displacements in the right panels of Fig. 4. The most advanced GR-M solution has correlation coefficients of only 0.4–0.5 with the horizontal NTOL predictions. In fact, for the 18 stations over November–December 2013, the horizontal correlation coefficients are less than 0.4 on average for the GR-M displacements. It shows that, compared to the vertical NTOL signals, the horizontal loading signals are usually too weak to stand out in the subdaily GNSS displacements.

Since the NTOL signals span a broad frequency band, the RMS statistics in Table 3 and Fig. 4 can, at most, act as a rough and simplistic measure for the subdaily GNSS resolution. In the next section, we therefore inspect the 3-hourly GNSS displacements in the time-frequency domain by means of wavelet analysis, in order to ascertain on what timescales the subdaily GNSS displacements are able to resolve NTOL signatures.

### 4.2 Wavelet analysis in the time-frequency domain

Compared to classic spectral analysis (*e.g.*, Bos et al., 2013; Langbein, 2017), wavelets can describe the temporal multiscale features of a nonstationary process, such as the NTOL signals in this study. By decomposing a time series in the time-frequency domain, wavelet analysis is able to localize its dominant modes of variability and determine how they evolve over time. We used Morlet wavelets and the wavelet transforms were realized according to Torrence and Compo (1998) who developed an easy-to-use toolkit including a statistical significance test.

The wavelet power spectra of station ALDB from timescales 0.25 to 24 days for the vertical component of the G, G-M, GR and GR-M displacements, as well as the NTOL predictions are shown in Fig. 5 (for the remaining 17 stations refer to Figs. S18-S34).

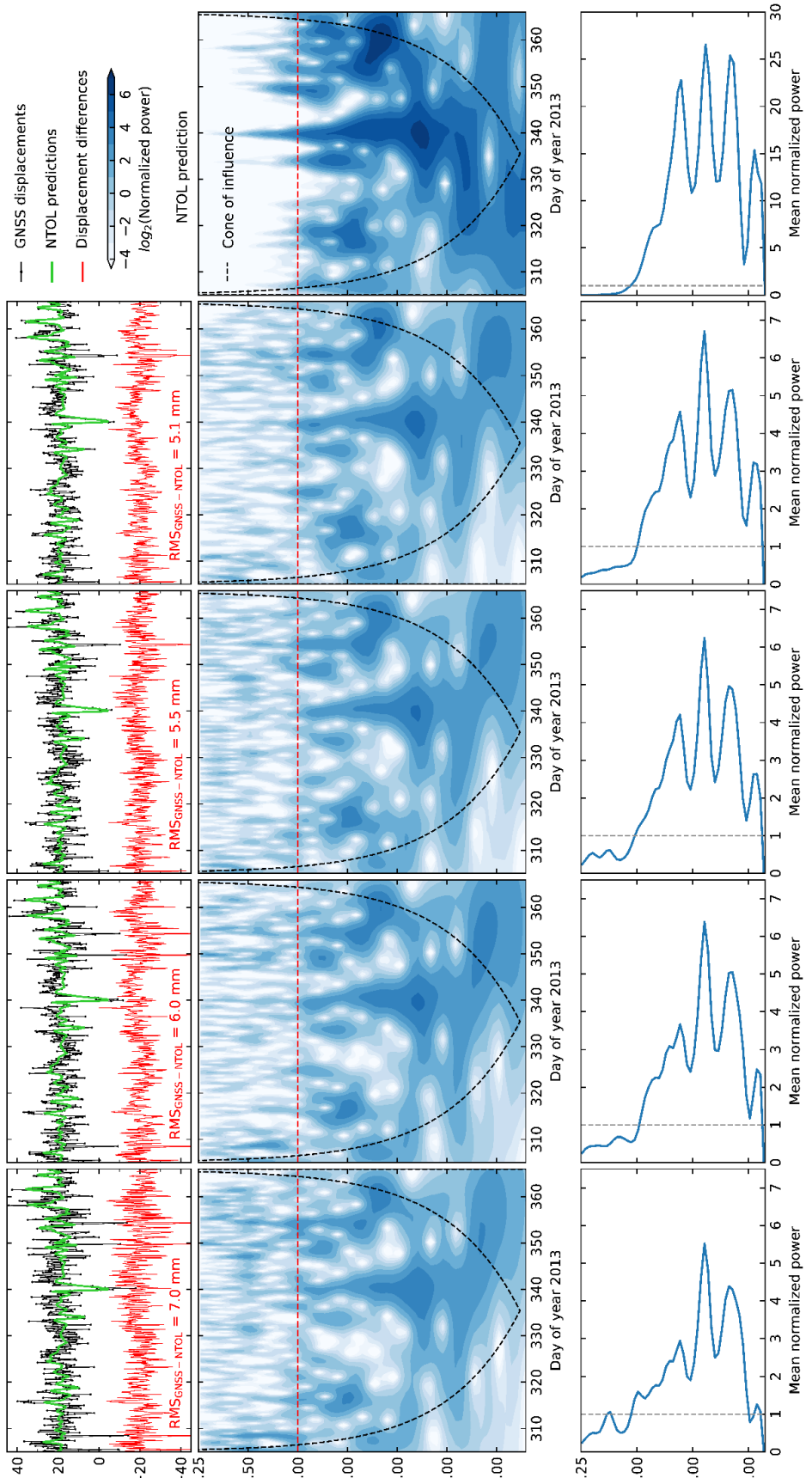


**Figure 5.** Wavelet power spectra for the 3-hourly vertical GNSS displacements and the hourly NTOL predictions at ALDB over November–December 2013. The top four panels exhibit the vertical GNSS displacements (black curves, offset by 20 mm) derived from the "G", "G-M", "GR" and "GR-M" solutions, which are overlaid with the NTOL predictions (green curves, offset by 20 mm). Their differences are displayed in red and offset by −20 mm. Correspondingly, the first four middle panels show the wavelet power spectra with the dashed black curves denoting the cone of influence (Torrence & Compo, 1998) and the dashed red lines indicating the 1-d timescale. The wavelet power spectra of NTOL predictions are plotted in the rightmost middle panel. All displacements are divided by their standard deviations to obtain normalized power spectra. For each type of displacements above, the bottom panels show the averaged power with respect to timescales from 0.25 to 24 days, and the vertical dashed lines denote 1 in particular. Note that only the powers enclosed within COI are counted and the rightmost bottom panel has a different horizontal axis range.

Note that the wavelet power spectra of NTOL signals were computed using their hourly predictions, but the power spectra over the 0.083–0.25-day (or 2–6 hours) timescales are almost null and thus ignored in the rightmost middle panel of Fig. 5. This also explains why it is the 3-hourly, rather than 1 or 2-hourly, GNSS displacements that are employed in this study. The top four panels for the GNSS displacements (black curves) are overlain with the NTOL predictions (green curves). Their differences are plotted in red. Though the top four plots echo Fig. 4 by showing the steady improvement of GNSS displacements, they barely demonstrate which day and over what timescale the GNSS displacements agree better with the NTOL predictions.

To localize such agreements, we divided the GNSS displacements and the NTOL predictions by their individual standard deviations to carry out normalized wavelet transforms and the resulting power spectra can be compared directly (Torrence & Compo, 1998). In particular, the darker the blue color is within the middle panels, the larger the wavelet power is or the more significant the corresponding signal is in contrast to the background signals or noise. Moreover, we also plotted the cone of influence (COI) outlined by dashed black curves within which the wavelet power spectra are trustworthy. Torrence and Compo (1998) pointed out that the edge effects caused by padding time series with zeros for the convenience of wavelet transforms discredit the wavelet power spectra outside the COI. If we focus on the rightmost middle panel exhibiting the wavelet power spectra for the NTOL predictions, most power is clearly concentrated on timescales over one day. The most conspicuous subdaily power spectra appear around day 340 on the occasion of the largest storm surge, after which pronounced subdaily powers are observed repeatedly during the second half of December.

In general, for the timescales over one day, all four GNSS wavelet power spectra successfully reproduce the major features of the wavelet powers of the NTOL predictions. The large power around day 340 with a timescale of 2–8 days, as well as those from day 350 to 365 for a timescale of 2–4 days, are all clearly visible in the first four middle panels of Fig. 5. As for the weaker NTOL signals near day 320 for the 2-day timescale, the GR and GR-M solutions show closer resemblance to the NTOL predictions than the G and G-M solutions in terms of wavelet powers.

However, the subdaily wavelet power spectra for the vertical GNSS displacements are chaotic. For the G solution, the subdaily power spectra for the NTOL signals around

day 340 and during the second half of December cannot be distinguished from the power spectra of other subdaily signals spreading across the two months. The application of multipath corrections (*i.e.*, G-M) cleans up part of the subdaily power spectra, especially those near the 0.5-day timescale through days 330–360. However, it is still hard to discriminate the power spectra of the NTOL signals contained within the GNSS displacements. The GPS/GLONASS integration (*i.e.*, GR) delivers similar power spectra improvement to that by the G-M solution, but seems to work better for the 0.25–1.00-day timescales near day 310 and through days 350–365. This improvement for the subdaily timescales can be further enhanced by applying multipath corrections (*i.e.*, GR-M). From a visual inspection on the fourth middle panel from the left, the power spectra of subdaily NTOL signals within GNSS displacements around day 340 are more visible. To quantify the power reduction over the subdaily timescales from the G to GR-M solutions, we plot along the bottom of Fig. 5 the averaged power for all timescales spanning 0.25–24 days with regard to each GNSS solution and the NTOL predictions. Only the power spectra enclosed within the COIs are counted. The G displacements have a peak power around 0.5-day timescale, but it disappears in the case of the other three solutions. Overall, the normalized subdaily powers (0.25–1 days) decrease by about 25% in both cases of the G-M and GR displacements, demonstrating the noise suppression capability of multi-GNSS integration.

Likewise, we plot the wavelet power spectra for the horizontal components of station ALDB in Fig. 6 (for the remaining 17 stations refer to Figs. S35–S51). The top panels show the horizontal displacements calculated using the east and north components. The ORT filtering and the addition of GLONASS data reduce the discrepancy (red curves) between the GNSS displacements and the NTOL predictions from 2.4 to 1.9 mm in terms of RMS errors. In general, the best agreement between the GNSS displacements and the NTOL predictions is over the timescale of 4–8 days, as shown by the middle panels of wavelets. Especially, the addition of GLONASS extends this agreement approximately to the timescale of 2 days. However, over the subdaily timescales, the power spectra of GNSS displacements do not show any resemblance to those of the NTOL predictions in the rightmost middle panel. This result might be due to the inaccurate horizontal NTOL predictions (*e.g.*, Earth model uncertainty) or insufficient GNSS precision to detect such minor horizontal NTOL signals.

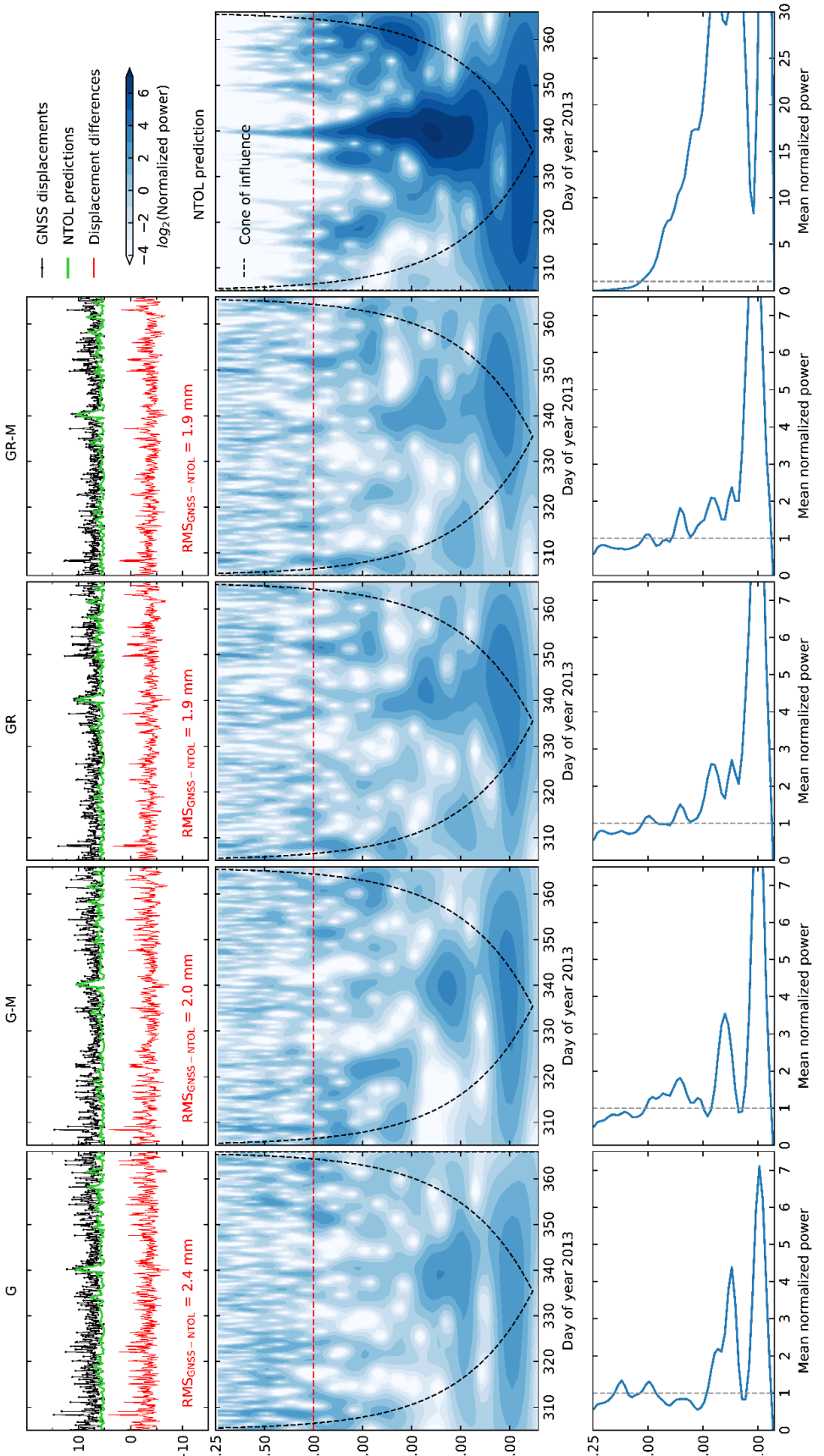


**Figure 6.** Wavelet power spectra for the 3-hourly horizontal GNSS displacements and the hourly NTOL predictions at ALDB over November–December 2013. We calculated the horizontal displacements using the east and north components. The meaning of each panel and symbol refer to those in Fig. 5. The color bar is the same as that in Fig. 5. Note that the curves in the top four panels are offset by ±5 mm.

### 4.3 Principal component analysis (PCA) for spatially coherent signals

Figs. 5 and 6 show that the 3-hourly GNSS displacements might still be too "noisy" over the subdaily timescales to identify the rich and diverse NTOL signatures. Fig. 2 has illustrated the coherent pattern of the NTOL predictions among the 18 coastal stations, which implies that their GNSS displacements should also reflect this coherence, unless the noise spectra are dominant and vary spatially. PCA is able to define an orthogonal coordinate system to describe optimally the variance of the GNSS displacements. In this case, the first few principal components can be used to describe the coherent pattern and the remaining components are presumed to be noise (Preisendorfer, 1988). We thus carry out PCA over the G, G-M, GR and GR-M displacements for the 18 stations with the goal of extracting the common NTOL signatures (Dong et al., 2006). The PCA is implemented using the scikit-learn module (ver. 0.18.1) from Python.

We recover the vertical displacements of the 18 stations using the first PC along with each station's spatial response. The normalized vertical spatial response to the first PC (or the normalized eigenvector of the first PC, *cf.*, Dong et al. (2006)) exceed 65% at all 18 stations. The first PC can explain 44%, 48%, 53% and 57% of the vertical variances for the G, G-M, GR and GR-M displacements, respectively. In contrast, the second PC explains less than 9%. Similar performance is achieved for the north component using the first PC. On the contrary, while the first PC for the east component explains about 40% of its variance and the normalized spatial response at all 18 stations exceed 65%, the second PC also explains about 17% of its variance and the mean absolute spatial response is around 55%. Referring to Figs. 2 and 3, the stations residing on the western and eastern coasts of the southern North Sea show roughly opposite displacement patterns for the east component, suggesting that the second PC also matters in the recovery of the east NTOL signals.

The PCA-recovered vertical GNSS displacements and their wavelet power spectra for station ALDB are shown in Fig. 7 (for the remaining 17 stations refer to Figs. S52–S68). We use the same color bar as that in Fig. 5 to facilitate cross comparisons. The top panels confirm that the PCA-recovered displacements do appear to have better agreement with the NTOL predictions than the original GNSS displacements, and the NTOL signals become more apparent within the GNSS displacements. The PCA assists in reducing the vertical discrepancy between the G displacements and the NTOL predictions

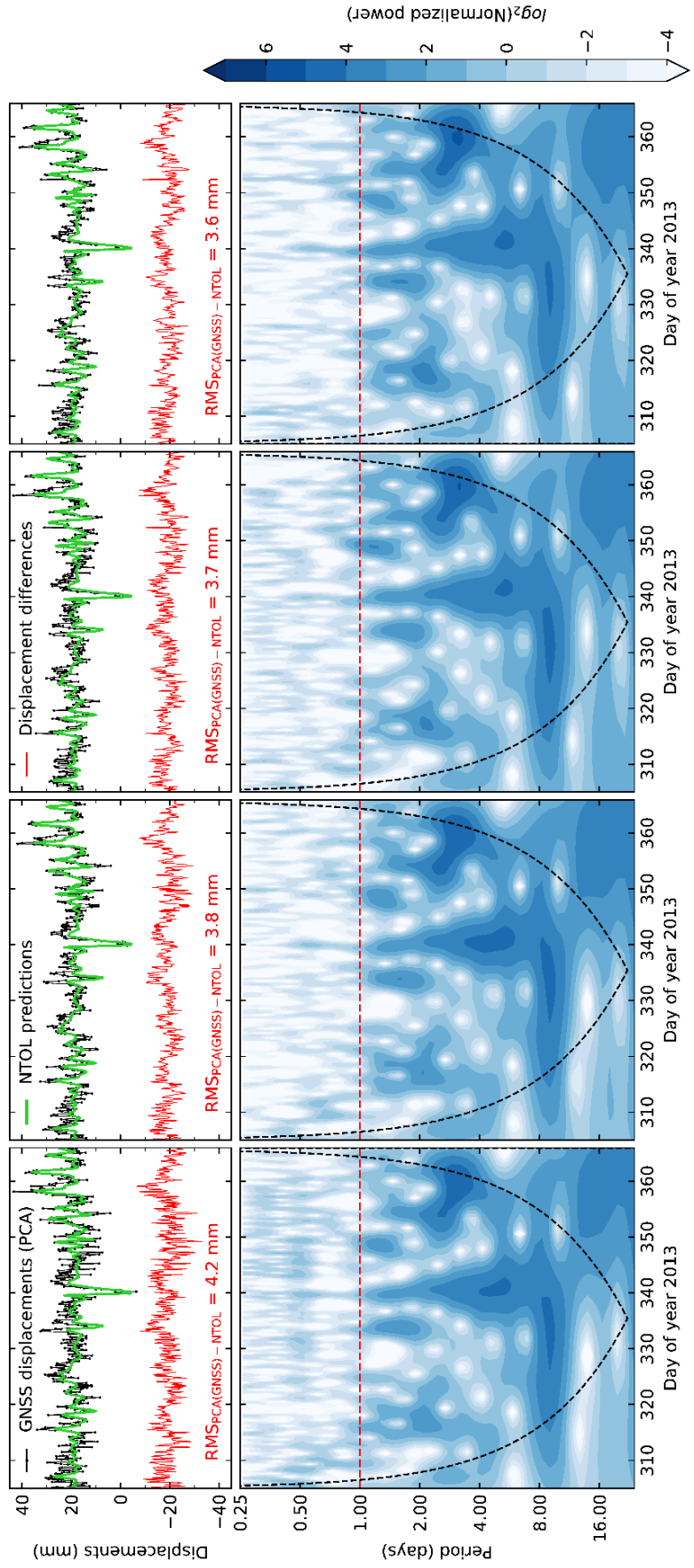


**Figure 7.** Wavelet power spectra of ALDB's two-month 3-hourly vertical displacements recovered from the principal component analysis (PCA) over the 18 coastal stations. The vertical displacements are recovered from the first PC. The meaning of each panel and symbol refer to those in Fig. 5. The color bar and the horizontal range of the bottom panels are the same as those in Figs. 5 and 6. The averaged powers larger than 7.5 are not plotted in the bottom panels.

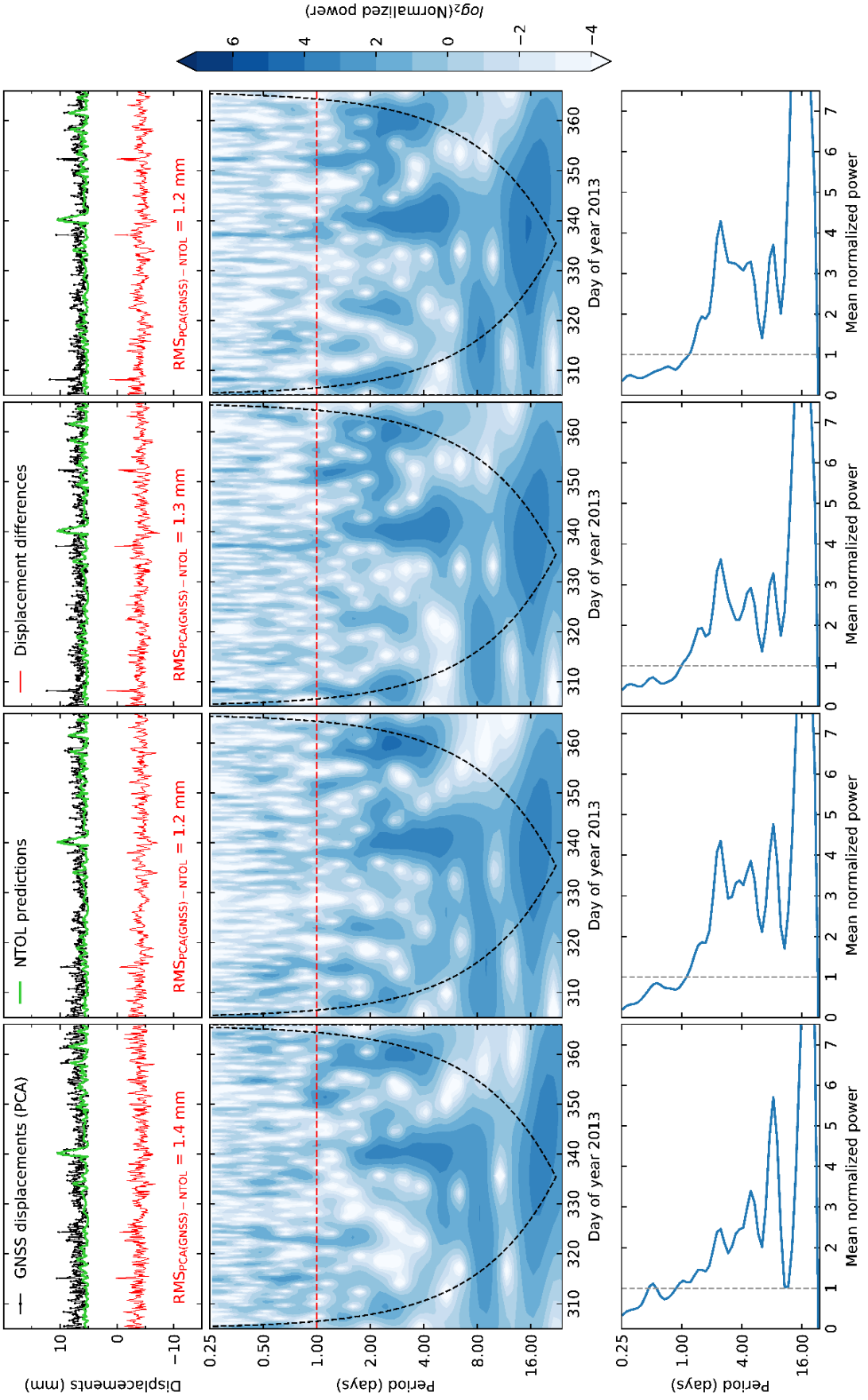


**Figure 8.** Wavelet power spectra of ALDB's two-month 3-hourly horizontal displacements recovered from PCA over the 18 coastal stations. Note that the north displacements are recovered from the first PC while the east recovered from the first plus the second PC. The meaning of each panel and symbol refer to those in Fig. 5. The color bar and the horizontal range of the bottom panels are the same as those in Figs. 5 and 6. The averaged powers larger than 7.5 are not plotted in the bottom panels.

by 40% from 7.0 to 4.2 mm in terms of RMS errors. With regard to the GR displacements, the RMS error also falls from 5.5 to 3.7 mm, outperforming the G-M solutions. In fact, such improvements hold at all 18 coastal stations for all four GNSS solutions as shown in the $\mathrm{RMS}_{\mathrm{PCA(GNSS)\text{-}NTOL}}$ column compared to the $\mathrm{RMS}_{\mathrm{GNSS\text{-}NTOL}}$ in Table 3.

Moreover, the wavelet power spectra for the vertical component over the subdaily timescales show closer agreement to those in rightmost middle panel of Fig. 5. Compared to the PCA(G) displacements, the PCA(G-M) displacements are quieter over the subdaily timescales, especially around 0.5 day. The NTOL signals around day 340 and those over days 350–365 are thus more visible with respect to the background signals/noise. Encouragingly, the PCA(GR) displacements have comparable performance to PCA(G-M) in recovering the subdaily NTOL signals. If the multipath corrections are further applied, the PCA(GR-M) displacements have even less "noisy" subdaily wavelet powers, which make the NTOL signals around day 340 and over days 350–365 more identifiable. This is a sharp contrast to the GNSS subdaily power spectra in Fig. 5. On average, the bottom panels of Fig. 7 show that the subdaily wavelet powers (mostly for noise) are reduced by more than 50% compared to those in Fig. 5. In addition, we reiterate that the PCA applied to the GR displacements is able to recover more precise NTOL displacements than that applied to the G displacements, even though the G solutions can be improved more by the PCA. This point can be verified by the wavelet power spectra of noise around the 0.5-day timescale, which are still visible in PCA(G) but almost disappear in PCA(GR).

Likewise, Fig. 8 displays the PCA-recovered horizontal displacements and their wavelet power spectra for station ALDB (for the remaining 17 stations refer to Figs. S69–S85). Specifically, the RMS of the differences between the G displacements and the NTOL predictions is reduced from 2.4 to 1.4 mm after the PCA is applied. Similarly, the RMS error for the GR displacements declines from 1.9 to 1.3 mm. Now the NTOL signatures around the 2-day timescale through days 350–365 are visible in both GR and GR-M solutions. Despite this improvement, it is disappointing that the subdaily wavelet power spectra in Fig. 8 are still "noisy". We cannot discriminate the subdaily NTOL signals around day 340 and over days 350–365 against others at various subdaily timescales. However, we should keep in mind that another plausible cause for this outcome is that the horizontal NTOL predictions are not accurate enough.

In addition, the PCA will recover not only the common-mode signals of interest, but also the common-mode errors (CMEs) which we hope to remove. Such CMEs can be ascribed to spatially correlated nuisance errors, *e.g.*, satellite orbit anomalies, satellite clock errors, residual atmospheric refractions, etc. The CMEs may then in part explain the remaining discrepancy between the GNSS displacements and the NTOL predictions. Therefore, the more sufficient the GNSS error mitigation is, the more accurate spatially coherent signals of interest can be gained from the PCA.

Finally, the sea levels varied drastically from hour to hour across the southern North Sea (*cf.*, Fig. 1), implying that the ensuing NTOL response at the 18 near-field stations might be subject to strong "local" effects and deviate remarkably from their nominal spatial response to the first PC (Dong et al., 2006). An extreme example is station HELG which is located on an island. Fig. S68 shows that the PCA-recovered vertical subsidence around day 340 is 50%, or 20 mm, smaller than the NTOL predictions, while in contrast Fig. S17 shows that this peak downward motion has actually been fully captured by the original GNSS displacements. One explanation is that the first vertical PC can only describe the common subsidence characteristics shared by all 18 stations, or in other words, can only reflect the phase-consistent variation of sea levels across the southern North Sea over the two months. Any local sea level excursions from this phase-consistency will disturb the spatial response of the near-field stations to the first PC. This fact highlights the intrinsic limitation of using the first few PCs to recover individual crustal motions.

## 5 Discussion

The 3-hourly GR-M displacements agree well with the NTOL predictions to a 5.7-mm RMS error in the vertical (Table 2), which appear to support the notion that GNSS displacements can resolve a 10-mm (approximately $2\sigma$) NTOL signal. However, this is not the case. We band-pass filter the NTOL predictions at ALDB at corner periods of 6–24 h to extract the subdaily signals, and the signals over 1 day are also extracted for comparison (Fig. 9). It can be seen that the peak-to-peak subdaily displacement in the vertical is about 10 mm around day 340 (black curves). This loading signature is however not discriminated within the subdaily wavelet power spectra for the vertical GNSS displacements in Fig. 5. In contrast, the 10-mm loading signature around day 316, as shown by the green curve for the vertical component in Fig. 9, is identified successfully over the 2-day timescale in the wavelet power spectra in Fig. 5. This comparison rein-

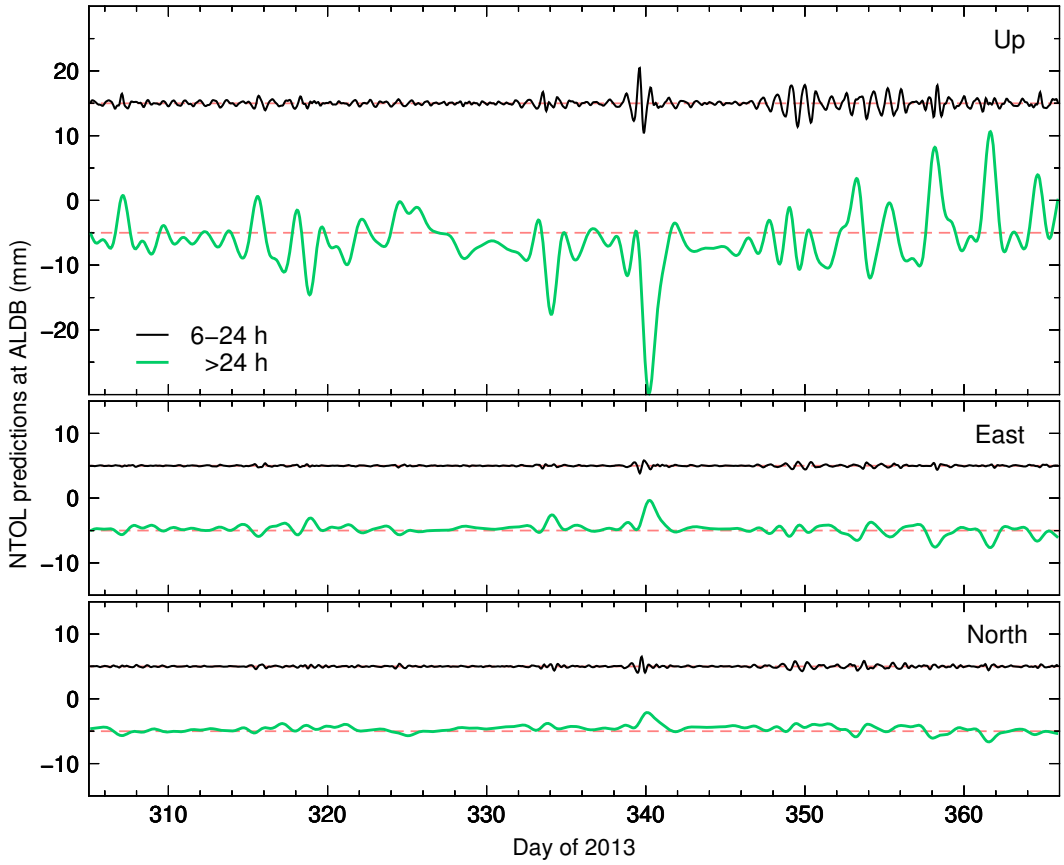


**Figure 9.** NTOL predictions (mm) filtered at corner periods of 6 and 24 hours for the up, east and north components at ALDB during November–December 2013. The black curves denote the band-pass (6–24 h) filtered displacements, and the green curves denote the low-pass (>24 h) filtered displacements. All curves are offset by multiples of 5 mm to avoid overlap of symbols.

forces that the RMS statistics are only an average precision measure, which should not always be used to quantify the GNSS displacement resolution.

The inability of 3-hourly GNSS in discriminating subdaily vertical signals of up to 10 mm is disappointing. Penna et al. (2015) and Martens et al. (2016a) reported that subdaily GPS could recover the near semi-diurnal OTL signals at a resolution of 0.2 mm. This appears far beyond the precision that can be expected for GPS displacements, since raw GPS carrier-phase noise is almost ten-fold higher than 0.2 mm. The explanation is that the harmonic analysis is imposed strictly on the subdaily GPS displacements. In detail, the OTL signals are modeled as periodic displacements since ocean tides are exceptionally well known from astronomical ephemerides; only a few parameters (*e.g.*, amplitude, Greenwich phase lag, etc.) need to be estimated in a harmonic fitting to the GPS displacements spanning multiple years. As a result, the harmonic coefficients can be computed with a very low formal uncertainty (*e.g.*, sub-millimeter level), favorably beyond the precision of individual epochs.

However, such strong model constraints are not always practical, as exemplified in the NTOL detection in this study. We did not introduce any NTOL models to fit the subdaily GNSS displacements, but retrieved the common-mode signals as the nominal NTOL signatures through the PCA by virtue of the spatial coherence among the 18 coastal stations (*cf.*, Figs. 7 and 8). In this manner, we reduced successfully the discrepancy between the GNSS displacements and the NTOL predictions, and the subdaily NTOL signatures become more visible in the wavelet power spectra. The PCA was also experimented on by Ji and Herring (2011, 2012) for the discrimination of transient inflations at the Akutan volcano, Alaska in early 2008 and groundwater loading in the San Gabriel Valley, California from 1998 until 2011. Despite such success in enhancing the subdaily GNSS resolution for transient motions, the PCA is at risk of absorbing common-mode or spatially coherent nuisance noise into the PC. In this study, such noise consists of satellite orbit and clock anomalies, residual atmospheric refractions, tidal loading and hydrological loading errors, etc.

## 6 Conclusions and outlook

In order to investigate the resolution of subdaily GNSS in discriminating transient crustal motions, we computed 3-hourly GPS/GLONASS solutions to identify the NTOL

signals at 18 coastal stations along the southern North Sea in Europe during November–December 2013. The predicted NTOL displacements can be up to 40 mm in the vertical and up to 5 mm in the horizontal components. We applied multipath corrections to the GPS/GLONASS solutions with the goal of achieving better subdaily positioning precision.

We found that the 3-hourly GNSS displacements agreed with the NTOL predictions to a mean RMS error of 5.7, 1.9 and 2.0 mm for the up, east and north components, respectively. The correlation coefficients between the GNSS vertical displacements and the NTOL predictions were up to 0.7 with an average of 0.6 over all 18 stations. Through a wavelet analysis in the time-frequency domain, 3-hourly GNSS could only marginally identify the most pronounced subdaily loading signature of 10-mm subsidence around day 340. Fortunately, the NTOL signals could be enhanced through the PCA on the 18 stations since they responded to NTOL almost unanimously over the two months. The PCA-recovered vertical GNSS displacements had an RMS error as low as 3.9 mm from the NTOL predictions, showing a 32% improvement compared to the original GNSS displacements. In the meantime, the subdaily NTOL signatures, especially those taking place during December 2013, could be identified more easily.

Although the PCA can enhance the subdaily NTOL signals by virtue of the spatial coherence among the coastal stations, it takes the risks of both assimilating common-mode noise into the crustal motions of interest and neglecting significant individual deformations caused by local effects. Therefore, we demonstrate that the foremost scheme to improve the subdaily GNSS resolution is to mitigate a variety of error sources, such as the atmosphere pressure loading using surface pressure of higher spatiotemporal resolution from ECMWF (Hersbach et al., 2019). Moreover, involving more GNSS such as Galileo and BeiDou into the high-precision positioning will be especially beneficial (*e.g.*, Geng et al., 2018). Finally, we envision that subdaily GNSS displacements, since they are an integrated signal of the loading across the whole North Sea, could be used to improve storm surge forecasting, especially in the interior of the North Sea where there is little or no constraint for example from tide gauges.

## Acknowledgments

This work is funded by National Key R&D Program of China (2018YFC1503601) and National Science Foundation of China (41861134009). It is also under the auspices of IAG

SC 4.4 "GNSS Integrity and Quality Control". We thank the IGS for the final satellite orbit and clock, and global ionosphere map products, and BIGF (British Isles continuous GNSS Facility) for the GNSS data within the UK. IGS data and products can be accessed publicly through https://cddis.nasa.gov/archive, while BIGF data can be requested freely from http://www.bigf.ac.uk. All computational work was finished on the high-performance computing facility at Wuhan University. The NTOL predictions, all raw GNSS displacements and the PCA-recovered GNSS displacements have been open-accessed in the Zenodo public repository (https://zenodo.org/record/3550717). We thank Matt King and another four anonymous reviewers for their valuable comments.

## References

Abbaszadeh, M., Clarke, P. J., & Penna, N. T. (2020). Benefits of combining GPS and GLONASS for measuring ocean tide loading displacement. *J. Geod.*, *94*, 63.

Agnew, D. C. (1997). NLOADF: a program for computing ocean-tide loading. *J. Geophys. Res.*, *102*, 5109-5110.

Agnew, D. C., & Larson, K. M. (2007). Finding the repeat times of the GPS constellation. *GPS Solut.*, *11*(1), 71-76.

Bilich, A., Cassidy, J. F., & Larson, K. M. (2008). GPS seismology: Application to the 2002 Mw 7.9 Denali fault earthquake. *Bull. Seismol. Soc. Am.*, *98*(2), 593-606.

Blewitt, G. (2003). Self-consistency in reference frames, geocenter definition, and surface loading of the solid Earth. *J. Geophys. Res.*, *108*(B2), 2103.

Bock, Y., Melgar, D., & Crowell, B. W. (2011). Real-time strong-motion broadband displacements from collocated GPS and accelerometers. *Bull. Seismol. Soc. Am.*, *101*(6), 2904-2925.

Boehm, J., Werl, B., & Schuh, H. (2006). Troposphere mapping functions for GPS and very long baseline interferometry from European Centre for Medium-Range Weather Forecasts operational analysis data. *J. Geophys. Res.*, *111*. doi: 10.1029/2005JB003629

Bos, M. S., Fernandes, R. M. S., Williams, S. D. P., & Bastos, L. (2013). Fast error analysis of continuous GNSS observations with missing data. *J. Geod.*, *87*(4), 351-360.

Choi, K., Bilich, A., Larson, K. M., & Axelrad, P. (2004). Modified sidereal filtering: Implications for high-rate GPS positioning. *Geophys. Res. Lett.*, *31*. doi: 10.1029/2004GL021621

Dill, R., Klemann, V., Martinec, Z., & Tesauro, M. (2015). Applying local Green's functions to study the influence of the crustal structure on hydrological loading displacements. *J. Geodyn.*, *88*(2015), 14-22.

Dong, D., Fang, P., Bock, Y., Webb, F., Prawirodirdjo, L., Kedar, S., & Jamason, P. (2006). Spatiotemporal filtering using principal component analysis and Karhunen-Loeve expansion approaches for regional GPS network analysis. *J. Geophys. Res.*, *111*(B3), 1581-1600.

Dong, D., Wang, M., Chen, W., Zeng, Z., Song, L., Zhang, Q., ... Lv, J. (2016). Mitigation of multipath effect in GNSS short baseline positioning by the multipath hemispherical map. *J. Geod.*, *90*(3), 255-262.

Dong, D., Yunck, T., & Heflin, M. (2003). Origin of the international terrestrial reference frame. *J Geophys Res*, *108*(B4), 2200.

Dziewonski, A. M., & Anderson, D. L. (1981). Preliminary reference Earth model. *Phys. Earth Planet. Inter.*, *25*, 297-356.

Farrell, W. E. (1972). Deformation of the Earth by surface loads. *Rev. Geophys.*, *10*, 761-797.

Flather, R. A. (2000). Existing operational oceanography. *Coastal Eng.*, *41*, 13-40.

Fratepietro, F., Baker, T. F., Williams, S. D. P., & Van Camp, M. (2006). Ocean loading deformations caused by storm surges on the northwest European shelf. *Geophys. Res. Lett.*, *33*(L06317).

Fritsche, M., Dietrich, R., Knöfel, C., Rülke, A., Vey, S., Rothacher, M., & Steigenberger, P. (2005). Impact of higher-order ionospheric terms on GPS estimates. *Geophys. Res. Lett.*, *32*(23), L23-311.

Geng, J., Chen, X., Pan, Y., Mao, S., Li, C., Zhou, J., & Zhang, K. (2019b). PRIDE PPP-AR: an open-source software for GPS PPP ambiguity resolution. *GPS Solut*, *23*(91).

Geng, J., Chen, X., Pan, Y., & Zhao, Q. (2019a). A modified phase clock/bias model to improve PPP ambiguity resolution at Wuhan University. *J. Geod.*, *93*(10), 2053-2067.

Geng, J., Jiang, P., & Liu, J. (2017). Integrating GPS with GLONASS for high-rate

seismogeodesy. *Geophys. Res. Lett.*, *44*. doi: 10.1002/2017GL072808

Geng, J., Pan, Y., Li, X., Guo, J., Liu, J., Chen, X., & Zhang, Y. (2018). Noise characteristics of high-rate multi-GNSS for subdaily crustal deformation monitoring. *J. Geophys. Res.*, *123*, 1987-2002.

Geng, J., Williams, S. D. P., Teferle, F. N., & Dodson, A. H. (2012). Detecting storm surge loading deformations around the southern North Sea using subdaily GPS. *Geophys. J. Int.*, *19*(2), 569-578.

Hammond, W. C., Blewitt, G., & Kreemer, C. (2016). GPS imaging of vertical land motion in California and Nevada: Implications for Sierra Nevada uplift. *J. Geophys. Res.*, *121*, 7681-7703. doi: 10.1002/2016JB013458

Herring, T. A., Melbourne, T. I., Murray, M. H., Floyd, M. A., Szeliga, W. M., King, R. W., ... Wang, L. (2016). Plate Boundary Observatory and related networks: GPS data analysis methods and geodetic products. *Rev. Geophys.*, *54*, 759-808. doi: 10.1002/2016RG000529

Hersbach, H., Bell, B., Berrisford, P., Horányi, A., Sabater, J. M., Nicolas, J., ... Dee, D. (2019). Global reanalysis: goodbye ERA-Interim, hello ERA5. *ECMWF Newsletter*, *159*, 17-24.

Ji, K. H., & Herring, T. A. (2011). Transient signal detection using GPS measurements: Transient inflation at Akutan volcano, Alaska, during early 2008. *Geophys. Res. Lett.*, *38*. doi: 10.1029/2011GL046904

Ji, K. H., & Herring, T. A. (2012). Correlation between changes in groundwater levels and surface deformation from GPS measurements in the San Gabriel Valley, California. *Geophys. Res. Lett.*, *39*. doi: 10.1029/2011GL050195

King, M. A., Watson, C. S., Penna, N. T., & Clarke, P. J. (2008). Subdaily signals in GPS observations and their effect at semiannual and annual periods. *Geophys. Res. Lett.*, *35*. doi: 10.1029/2007GL032252

Langbein, J. (2017). Improved efficiency of maximum likelihood analysis of time series with temporally correlated errors. *J. Geod.*, *91*(8), 985-994.

Larson, K. M., Bodin, P., & Gomberg, J. (2003). Using 1-Hz GPS data to measure deformations caused by the Denali fault earthquake. *Science*, *300*(5624), 1421-1424.

Larson, K. M., Poland, M., & Miklius, A. (2010). Volcano monitoring using GPS: Developing data analysis strategies based on the June 2007 Kīlauea Volcano

intrusion and eruption. *J. Geophys. Res.*, *115*, B07406.

Lyard, F., Lefevre, F., Letellier, T., & Francis, O. (2006). Modelling the global ocean tides: modern insights from FES2004. *Ocean Dynam.*, *56*(5), 394-415.

Malservisi, R., Schwartz, S. Y., Voss, N., Protti, M., Gonzalez, V., Dixon, T. H., ... Voyenko, D. (2015). Multiscale postseismic behavior on a megathrust: The 2012 Nicoya earthquake, Costa Rica. *Geochem. Geophys. Geosyst.*, *16*, 1848-1864. doi: 10.1002/2015GC005794

Martens, H. R., Rivera, L., Simons, M., & Ito, T. (2016b). The sensitivity of surface mass loading displacement response to perturbations in the elastic structure of the crust and mantle. *J. Geophys. Res.*, *121*, 3911-3938.

Martens, H. R., Simons, M., Owen, S., & Rivera, L. (2016a). Observations of ocean tidal load response in South America from subdaily GPS positions. *Geophys. J. Int.*, *205*, 1637-1664.

Matviichuk, B., King, M., & Watson, C. (2020). Estimating ocean tide loading displacements with GPS and GLONASS. *Solid Earth*, *11*, 1849-1863.

Melbourne, T. I., Webb, F. H., Stock, J. M., & Reigber, C. (2002). Rapid postseismic transients in subduction zones from continuous GPS. *J. Geophys. Res.*, *107*(B10).

Penna, N. T., Clarke, P. J., Bos, M. S., & Baker, T. F. (2015). Ocean tide loading displacements in western Europe: 1. Validation of kinematic GPS estimates. *J. Geophys. Res.*, *120*, 6523-6539.

Petit, G., & Luzum, B. (Eds.). (2010). *IERS Conventions (2010).* Frankfurt am Main, Germany: Verlag des Bundes für Kartographie und Geodäsie.

Pireaux, S., Defraigne, P., Wauters, L., Bergeot, N., Baire, Q., & Bruyninx, C. (2010). Higher-order ionospheric effects in GPS time and frequency transfer. *GPS Solut.*, *14*(3), 267-277.

Prates, G., García, A., Fernández-Ros, A., Marrero, J. M., Ortiz, R., & Berrocoso, M. (2013). Enhancement of sub-daily positioning solutions for surface deformation surveillance at El Hierro volcano (Canary Islands, Spain). *Bull. Volcanol.*, *75*(6), 724.

Preisendorfer, R. W. (1988). Principle component analysis in meteorology and oceanography. In C. D. Mobley (Ed.), *Develop. atmos. sci.* (Vol. 17, p. 425). New York: Elsevier.

Rebischung, P., Altamimi, Z., Ray, J., & Garayt, B. (2016). The IGS contribution to ITRF2014. *J. Geod.*, *90*(7), 611-630.

Reuveni, Y., Kedar, S., Owen, S. E., Moore, A. W., & Webb, F. H. (2012). Improving sub-daily strain estimates using GPS measurements. *Geophys. Res. Lett.*, *39*, L11311.

Shen, Z.-K., King, R. W., Agnew, D. C., Wang, M., Herring, T. A., Dong, D., & Fang, P. (2011). A unified analysis of crustal motion in Southern California, 1970-2004: The SCEC crustal motion map. *J. Geophys. Res.*, *116*, B11402.

Smalley Jr., R. (2009). High-rate GPS: How high do we need to go? *Seismol. Res. Lett.*, *80*(6), 1054-1061.

Spencer, T., Brooks, S. M., Evans, B. R., Tempest, J. A., & Möller, I. (2015). Southern North Sea storm surge event of 5 December 2013: Water levels, waves and coastal impacts. *Earth-Sci. Rev.*, *146*(2015), 120-145.

Torrence, C., & Compo, G. P. (1998). A practical guide to Wavelet analysis. *B. Am. Meteorol. Soc.*, *79*(1), 61-78.

Twardzik, C., Vergnolle, M., Sladen, A., & Avallone, A. (2019). Unravelling the contribution of early postseismic deformation using sub-daily GNSS positioning. *Sci. Rep.*, *9*, 1775. doi: 10.1038/s41598-019-39038-z

van Dam, T., Collilieux, X., Wuite, J., Altamimi, Z., & Ray, J. (2012). Nontidal ocean loading: amplitudes and potential effects in GPS height time series. *J. Geod.*, *86*(11), 1043-1057.

van Dam, T., Olivier, F., Wahr, J., Khan, S. A., Bevis, M., & Broeke Van Den, M. R. (2017). Using GPS and absolute gravity observations to separate the effects of present-day and Pleistocene ice-mass changes in South East Greenland. *Earth Planet Sci. Lett.*, *459*(2017), 127-135.

Wang, H., Xiang, L., Jia, L., Jiang, L., Wang, Z., Hu, B., & Gao, P. (2012). Load Love numbers and Greens functions for elastic Earth models PREM, iasp91, ak135, and modified models with refined crustal structure from Crust 2.0. *Comput and Geosci*, *49*(12), 190-199.

Williams, S. D. P., & Penna, N. T. (2011). Non-tidal ocean loading effects on geodetic GPS heights. *Geophys. Res. Lett.*, *38*, L09314.

Yuan, L., Chao, B. F., Ding, X., & Zhong, P. (2013). The tidal displacement field at Earth's surface determined using global GPS observations. *J. Geophys. Res.*,

*118*, 2618-2632.

Zumberge, J. F., Heflin, M. B., Jefferson, D. C., Watkins, M. M., & Webb, F. H. (1997). Precise point positioning for the efficient and robust analysis of GPS data from large networks. *J Geophys Res*, *102*(B3), 5005-5017.